Chapter 31

Design of Radial *p–i–n* Silicon Nanowires for High-Performance Solar Cells

Binh-Minh Nguyen and Jinkyoung Yoo
Center for Integrated Nanotechnologies, Los Alamos National Laboratory,
Los Alamos, New Mexico, USA

Shadi A. Dayeh
Center for Integrated Nanotechnologies, Los Alamos National Laboratory,
Los Alamos, New Mexico, USA and Department of Electrical and Computer
Engineering, University of California, San Diego, La Jolla, California, USA

Paul Schuele and David Evans
Sharp Laboratories of America, Camas, Washington, USA

S. Tom Picraux
Center for Integrated Nanotechnologies, Los Alamos National Laboratory,
Los Alamos, New Mexico, USA

31.1 Introduction

The quantum efficiency of solar cells, like that of any photon detector, is dictated by the ability to absorb photons to create conducting carriers, and the efficiency to drive such carriers to electrodes for collection. Having a medium that enables full photon absorption in a short length, together with a long carrier lifetime that allows photogenerated carriers to reach electrodes before recombining is ideal but is not always realistic. For example, silicon photovoltaics, despite being a major player in the solar cell market, suffer from their low absorption coefficient, thus requiring a thick absorbing layer that impairs the efficiency with which photogenerated carriers are collected. Radial *p–i–n* silicon nanowires (NWs) have been proposed as a candidate for reducing the optical absorption length and required processing purity in silicon-based solar cells without compromising their quantum efficiency and yet reducing the overall cell cost.[1] In this scheme incident light propagates along the axial dimension of the NWs and thus has a greater chance of being absorbed when the NW length extends beyond 10 μm due to interarray light scattering effects [Fig. 31.1(a)]. At the same time, the core–shell radial *p-i-n* structure leads electrical current flow along submicron radii, enabling rapid collection of most photogenerated carriers, as the transport length is typically less than the diffusion lengths of minority carriers [Fig. 31.1(b)].

Since the first discussion on the device operation of a radial NW geometry for photovoltaic cell,[1] much work has been done to experimentally realize the advantages of this NW array system.[2–14] A detailed survey on current activities and progress on NW array solar cells can be found in Ref 15. In the current work discussed in the chapter we perform finite-difference time-domain (FDTD) simulations to investigate the absorption process in arrayed

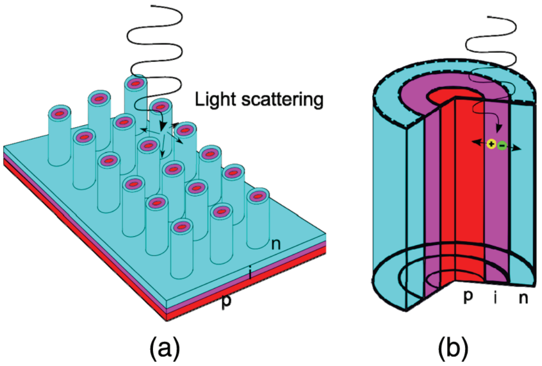

Figure 31.1 Schematic illustration showing the advantages of a core–shell NW solar cell. (a) Array arrangement enhances light scattering and photon absorption. (b) Short collection length of charge carriers along radial direction is decoupled from the long absorption length along the axis.

radial NWs. The goal of this work is to gain insight on absorption processes in NW arrays and to develop strategies for enhancing absorption efficiency. The effects of light scattering and the material filling ratio (ratio of the cross-sectional area that is occupied by the nanowires to the total area of the array) at different NW spacings will be discussed. Evolution of absorption with NW length, particularly in the long-wavelength range (700–1100 nm) will be shown to illustrate the advantages of NWs as opposed to conventional planar structures. In addition, actual NW geometries after shell overgrowth using chemical vapor deposition (CVD) for different NW lengths and spacings have been studied.

31.2 Device Fabrication

As discussed, the goal of this chapter is to present a theoretical estimation of absorption and external quantum efficiency of arrayed NW solar cells in order to guide experimental work. However, before going into the simulation details, it is important to know the capability of current fabrication technology so that devices to be simulated are experimentally feasible.

As described above, the device structure consists of two parts: the core and the shell. The core can be fabricated either with a bottom-up approach using the traditional vapor–liquid–solid (VLS) growth mode for NWs, or with a top-down approach by dry etching. The formation of the shell can also be done with either dopant diffusion/implantation/evaporation or lateral overgrowth using the vapor–solid growth mode. Approaches for core and shell fabrication can be flexibly combined, but the main objective is to realize an array of (preferentially vertical) NWs with sharp junction interfaces and sufficiently high material quality: minority carrier diffusion lengths larger than the device's diameter, yet a few orders of magnitude shorter than in bulk silicon solar cells.

In this work, for NW core formation, we utilize the top-down approach for NW array fabrication. A dielectric (SiO_2) or metal (Ni) mask is patterned on a piece of Si (111) substrate using electron beam (e-beam) lithography and CVD or e-beam metal evaporation, respectively. E-beam lithography is employed for its flexibility in altering mask designs during the optimization process. The NW diameter is typically in the range of few hundreds of nanometers to several micrometers, while the spacing between NWs can be as short as 1 μm without causing additional difficulties in NW formation using silicon deep reactive-ion etching [Fig. 31.2(a)]. NWs with a height of $\sim$10 μm are routinely used in this study; longer NWs (up to 20 μm) can be achieved with spacing larger than 2 μm. One advantage of a top-down approach is the ability to achieve up-straight NWs with tailorable sidewall profiles: vertical or conical. Top-down arrays also have more flexibility in controlling NW location, spacing, and a wide range of diameters. Bottom-up VLS growth can

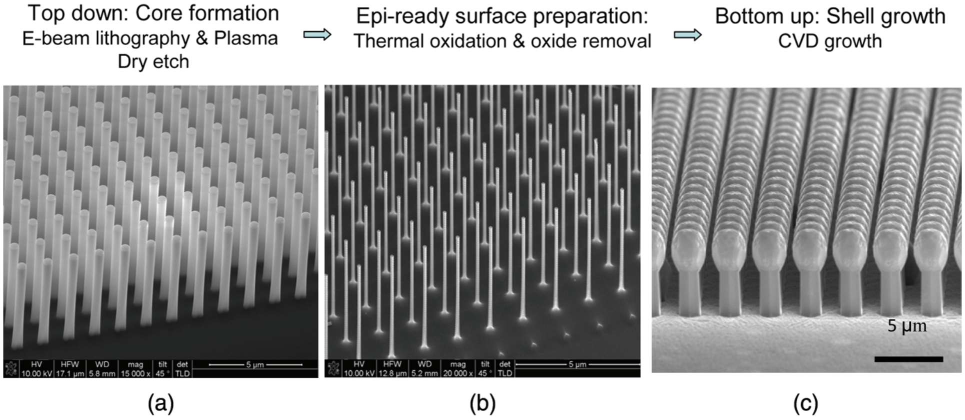

(a) (b) (c)

Figure 31.2 Illustration of NW solar cell fabrication process: (a) core formation, (b) surface damage removal, and (c) junction formation by vapor–solid shell overgrowth.

also enable control over NW location and spacing by using patterned metal catalysts but experiences difficulty in tuning growth conditions for a wide range of NW diameters to achieve high yield in vertically aligned NW arrays. The challenge for a top-down process is sidewall damage and residual contamination during plasma etching, which hamper the nucleation of the high-quality single-crystalline NW shell. In order to eliminate such detrimental defects, after the etch mask removal, the NW array is subjected to several cycles of a thermal oxidation step to create a thin oxide layer followed by a wet oxide etch step. The process also helps in removing sidewall undulation (scallops) due to the cyclic Bosch etch process [Fig. 31.2(b)]. From the smooth silicon surface on NW sidewalls, a single- crystalline radial shell can be grown by SiH_4-based CVD.[16]

The combination of top-down core etching and CVD shell growth enables both *p–n* and *n–p* core–shell polarity with controlled doping concentration and junction abruptness [Fig. 31.2(c)]. It also allows *i* regions of arbitrary thicknesses to be inserted between the *p* and *n* regions, if desired. After shell growth, one metal contact is deposited at the backside of the substrate, while the other is placed on the top grown layer, outside of the array area. Ideally, a transparent contact that fully covers the array is desired for perfect electrical access to each individual NW, but for process simplicity, a side contact pad is sufficient, as long as the shell doping is high enough for good electrical conduction and the core and the shell are not too thin to be fully depleted. The next section will investigate the relationship between doping concentration, core–shell thicknesses, and applied voltage to satisfy the above conditions.

After processing, the NW array is characterized with standard techniques[16] to extract quantum efficiency and device efficiency. An example of the external quantum efficiency of a silicon core–shell NW array cell is shown in

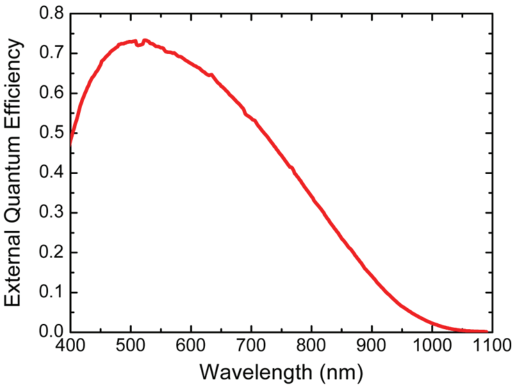

Figure 31.3 Measured external quantum efficiency of a solar cell based on a silicon NW array with 10-μm length, 3-μm wire-to-wire spacing, and 1.6-μm NW diameter.

Fig. 31.3. While the structure is far from optimal, a peak external quantum efficiency of 70% is already achieved. The goal of this chapter is to elucidate absorption processes in a NW array, and suggest an optimization scheme for even higher quantum efficiency.

31.3 Estimation of Depletion Region

One advantage of core–shell NW photovoltaics is the decoupling of electrical transport length from optical absorption length. NWs can be axially extended to fully absorb the incident light while photogenerated carriers are collected along radial directions with a transport length less than the NW radius. We assume here that the NW material is of a quality that allows the diffusion lengths of minority charge carriers to be a few times larger than the radius of the NWs. In other words, NWs can be fabricated with diameters smaller than the minority carrier diffusion length. In such conditions, all photogenerated carriers are collected to the electrodes and contribute to the photocurrent; thus, the diffusion transport of minority carriers is not of concern. The remaining challenge would be to minimize series resistance in the quasi-neutral regions between space-charge regions and the collecting electrodes.

Since there must be a conduction channel from the p and n regions at the core and surface of the NWs to the electrodes, the p and n regions cannot be fully depleted. To see under which conditions p–n regions become depleted, we look at the static picture of the charge–electric field distribution in the core–shell structure. Figure 31.4(a) is the schematic cross section of an n–p core–shell NW. An n-doped core of radius a and a p-doped shell of radius b have doping concentrations N_D and N_A, respectively. The depletion region is confined in a ring of inner radius r_n in the n-type core and outer radius r_p in the p-type shell. The electric field E and potential profile are obtained by

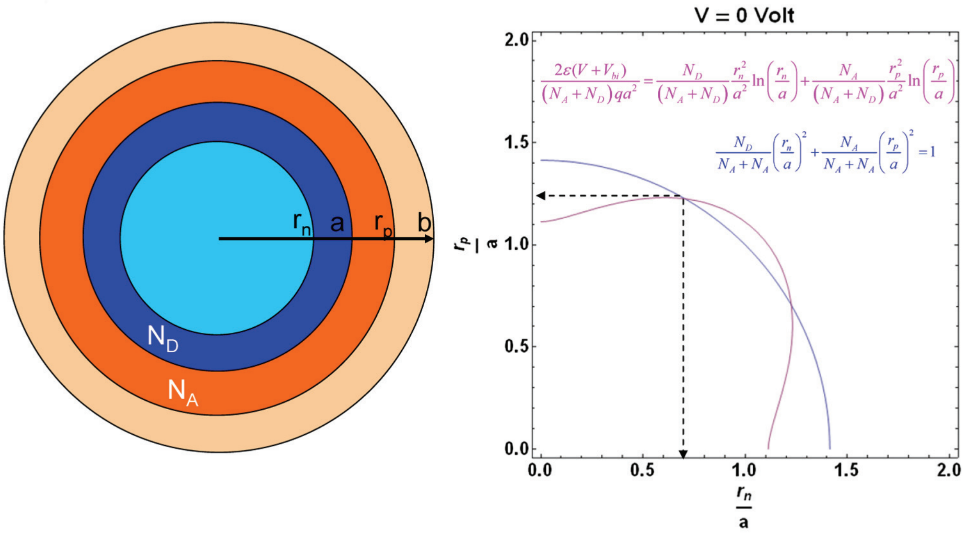

(a) (b)

Figure 31.4 (a) Schematic cross section of the core–shell NW structure. (b) Graphical solution to Eqs. (31.3) and (31.6) for a silicon NW with $a = 100$ nm, $V_{bi} = 1$ V, $V = 0$ V, $N_A = N_D = 10^{18}$ cm^{-3}.

solving the Poisson equation, similar to the case of 1D linear *p*-*n* junction, except in the NW case, the Poisson equation is 1D in cylindrical coordination. The charge density ρ is given by

$$\rho = \varepsilon\nabla E = \begin{cases} qN_D \text{ for } r_n \le r \le a \\ qN_A \text{ for } a \le r \le r_p \end{cases}, \tag{31.1}$$

where ε is the dielectric constant of the material, and q is the electron charge.

The first equation that links r_n and r_p is dictated by the charge neutrality condition:

$$\pi(a^2 - r_n^2)qN_D = \pi(r_p^2 - a^2)qN_A, \tag{31.2}$$

or

$$\frac{N_D}{N_A + N_D}\left(\frac{r_n}{a}\right)^2 + \frac{N_A}{N_A + N_D}\left(\frac{r_p}{a}\right)^2 = 1. \tag{31.3}$$

By taking the integral for ρ, with boundary conditions $E(r_n) = E(r_p) = 0$, we obtain

$$E = \begin{cases} \frac{1}{2}\frac{qN_D}{\varepsilon}\frac{r^2 - r_n^2}{r} \text{ for } r_n \le r \le a, \\ \frac{1}{2}\frac{qN_A}{\varepsilon}\frac{r_p^2 - r^2}{r} \text{ for } a \le r \le r_p. \end{cases} \tag{31.4}$$

A second integral of E will give the potential drop between $r = r_n$ and $r = r_p$, which is the sum of the built-in voltage V_{bi} and the applied reverse bias V:

$$\frac{2\varepsilon(V_{bi} + V)}{q} = N_D r_n^2 \ln\left(\frac{r_n}{a}\right) + N_A r_p^2 \ln\left(\frac{r_p}{a}\right), \tag{31.5}$$

or in a unitless form

$$\frac{2\varepsilon(V_{bi} + V)}{(N_A + N_D)qa^2} = \frac{N_D}{(N_A + N_D)} \frac{r_n^2}{a^2} \ln\left(\frac{r_n}{a}\right) + \frac{N_A}{(N_A + N_D)} \frac{r_p^2}{a^2} \ln\left(\frac{r_p}{a}\right). \tag{31.6}$$

A graphical solution to Eqs. (31.3) and Eqs. (31.6) is presented in Fig. 31.4(b). r_n and r_p are determined at the intersection of the two curves represented by the two equations. As discussed above, the n core and p shell must not be completely depleted, meaning that $r_n > 0$ and $r_p < b$. These conditions lead to certain constraints to the sum of the applicable bias and the built-in voltage. Although a solar cell operates at zero bias, these constraints would still apply, as the built-in voltage can be nearly the cell's energy gap, which is in order of 1 eV.

If the shell is thin, it would become depleted before the core becomes fully depleted. In this case, $r_p = b$, and the applied voltage cannot be larger than a threshold V_1, given by

$$\frac{2\varepsilon(V_{bi} + V_1)}{(N_A + N_D)qa^2} = \frac{N_D}{(N_A + N_D)} \frac{r_{n,\max}^2}{a^2} \ln\left(\frac{r_{n,\max}}{a}\right) + \frac{N_A}{(N_A + N_D)} \frac{b^2}{a^2} \ln\left(\frac{b}{a}\right), \tag{31.7}$$

where $r_{n,\max} = \sqrt{\frac{N_A + N_D}{N_D} - \frac{N_A}{N_D}\left(\frac{b}{a}\right)^2}\, a.$

If the shell is thicker, a higher voltage can be applied until the core is fully depleted: $r_n = 0$ when $r_p = r_{p,\max} \leq b$, and $V = V_2$, given by

$$r_{p,\max} = \sqrt{\frac{N_A + N_D}{N_A}}\, a \leq b, \tag{31.8}$$

and

$$\frac{2\varepsilon(V_{bi} + V_2)}{q} = N_A r_{p,\max}^2 \ln\left(\frac{r_{p,\max}}{a}\right) = \frac{1}{2}(N_A + N_D) \ln\left(\frac{N_A + N_D}{N_D}\right) a^2. \tag{31.9}$$

Such constraints between a, b, and V are summarized graphically in Fig. 31.5.

We have seen that for a given configuration of core and shell radii, the applied voltage must satisfy certain constraints to avoid full depletion in the core and shell regions. Reciprocally, for a solar cell operating at zero bias and a fixed doping concentration that determines V_{bi}, the core and shell radius must exceed the minimum values $a_{\min}$ and $b_{\min}$ so that neither the core nor the

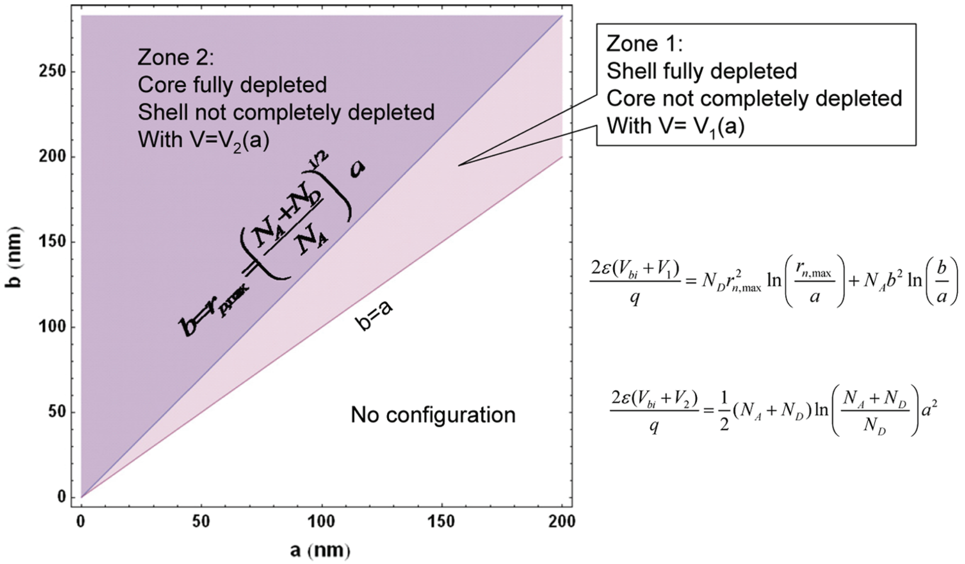

Figure 31.5 Correlation between core–shell thicknesses and junction depletion. Zone 1: When $V < V_1$, neither the core nor the shell are fully depleted. When $V = V_1$, the shell is fully depleted. Zone 2: When $V < V_2$, neither the core nor the shell are fully depleted. When $V = V_2$, the core is fully depleted.

shell is fully depleted. From Eq. (31.9), the minimum core radius can be derived as

$$a_{\min} = \sqrt{\frac{4\varepsilon V_{bi}}{q(N_A + N_D)\ln\left(\dfrac{N_A + N_D}{N_D}\right)}}, \tag{31.10}$$

and the minimum shell radius must be

$$b_{\min} = \sqrt{\frac{N_A + N_D}{N_A}}a_{\min} = \sqrt{\frac{4\varepsilon V_{bi}}{qN_A \ln\left(\dfrac{N_A + N_D}{N_D}\right)}}. \tag{31.11}$$

Numerically, if we assume that the core and shell of silicon NWs are doped at $N_A = N_D = 10^{18}$ cm^{-3}, we have $V_{bi} = \sim 1$ V, and the critical core–shell radii are 44 nm and 62 nm, respectively. In order to achieve an effective conduction channel to the electrodes, the actual radii of NWs should be larger than the critical values by tens of nanometers.

In the case of a *p–i–n* radial junction, if the *i* region is thick enough, all of the built-in potential and applied bias will drop at the *I* region, with a very thin depletion into the *p* and *n* regions. For example, an *i* region of 60-nm in length is enough to bear a built-in voltage of 1 V with only 20-nm depletion into the *n* region and 10-nm depletion into the *p* region, assuming that $N_A = N_D = 10^{18}$ cm^{-3} and $a = 100$ nm. In such cases, contact depletion is not a concern.

31.4 Optical Absorption Simulation

In order to assess the absorption process in NW arrays, we utilize FDTD solutions using the Lumerical Solutions, Inc. software package.[17] This commercial software is based on the FDTD framework to solve Maxwell's equations and calculate light–matter interactions. Optical properties [$n(\lambda)$, $k(\lambda)$] of bulk silicon are taken from Ref 18. The discrepancy in $n(\lambda)$, $k(\lambda)$ between simulation-database and actual values of silicon NWs, as well as experimental uncertainties in NW array fabrication (diameter uniformity, sidewall roughness, random fluctuation of NW length, etc.), might lead to some deviation of simulation results from experimental measurement; however, these discrepancies should not affect the physics and the array configuration dependencies under investigation.

Figure 31.6 is a schematic layout of the NW array to be simulated. Light–matter interaction is considered over the whole array with a primitive square lattice; however, to reduce the simulation cost, calculations are carried over only one unit cell containing one NW by utilizing appropriate periodic boundary conditions. With certain symmetries of the NW array and incident light, the calculation time and memory can be even further reduced by dividing the simulation volume by symmetric planes. Graphic cartoons shown in this section sketch only one NW but should be interpreted as the entire array of interacting NWs. The output of the simulation can be represented in different ways. One can monitor the temporal propagation of the incident-pulsed wave packet, comparing the electromagnetic field distribution at different times (Fig. 31.7). The Fourier transform of the temporal propagation intensity across a monitor plane represents the wavelength-dependent field intensity, from which one can determine reflection R, transmission T, and absorption or loss ($1 - R - T$) of a volume of material of interest [Fig. 31.7(b)]. Furthermore, the spatial dependence of the absorption at a particular wavelength can also be calculated [Fig. 31.7(c)]. The combination of

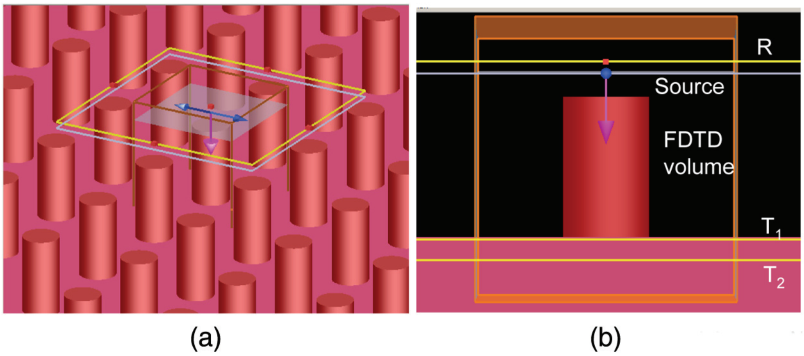

Figure 31.6 (a) Schematic layout of the NW array. (b) Simulation volume containing one NW; R, T_1, and T_2 are monitor planes for reflection and transmission, respectively.

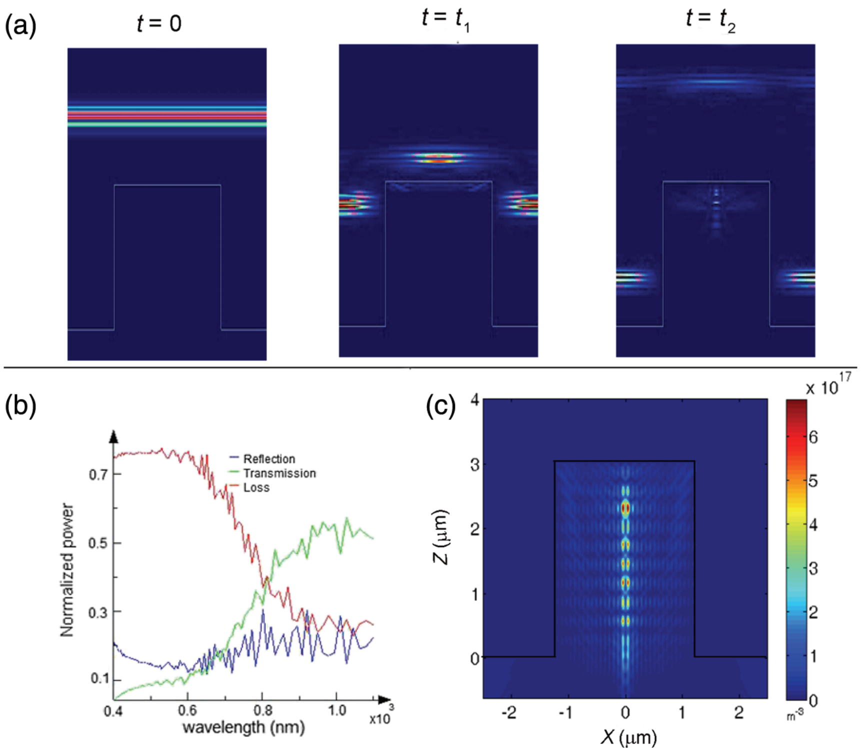

Figure 31.7 a) Snapshots taken at $t = 0$, $t = t_1$, and $t = t_2 > t_1$ illustrating temporal field propagation. (b) Wavelength-dependent spectra of field intensity. (c) Spatial absorption along a slice through the center of a NW. The scale bar indicates the absorption per unit volume in m^{-3}. (See color plate section.)

temporal, spectral, and spatial distributions of field intensity allows us to gain thorough insight into the absorption process and its dependence on NW array geometry, which will be discussed below.

31.4.1 Effect of nanowire length

It is expected that arrayed NW solar cells not only possess good efficiency in collecting photogenerated carriers to electrodes, but they also have enhanced absorption due to light scattering over the patterned structure. Under visible white light, an etched NW array appears darker than the unpatterned reference area, indicating that it absorbs more light. However, that apparently large absorption includes the absorption from both the NW array and the substrate underneath, but only photogenerated carriers in the NW array can contribute to electrical signal. It is thus important to isolate the absorption inside the NW array from the total absorption of the array and assess its dependence on the array geometry.

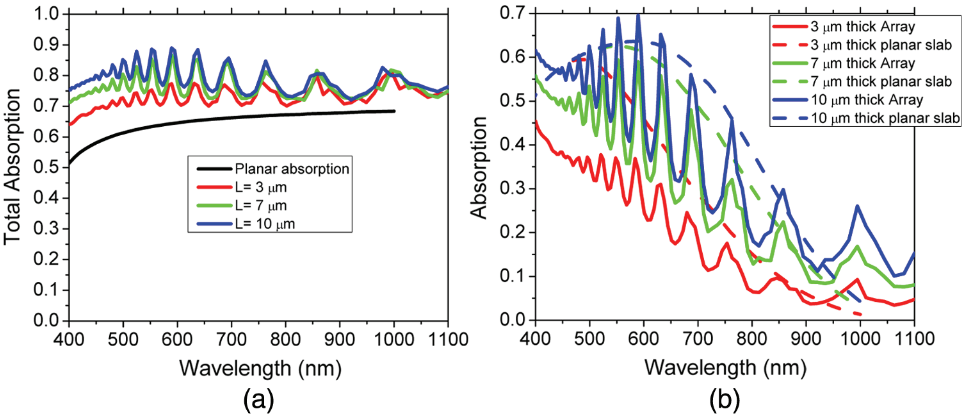

Figure 31.8 (a) Total absorption (NW + substrate) of simulated NW arrays compared to total absorption of an infinitely deep planar structure. (b) Absorption of NW arrays compared only to absorption of planar bulks with the same thickness. (See color plate section.)

Numerical simulation is performed for silicon NW arrays with spacing of 3 μm and NW diameter of 1.6 μm. The NW lengths are 3, 7, and 10 μm respectively. Figure 31.8(a) plots the total absorption ($1 - R$ with the notation in Fig. 31.6) of NW arrays with different lengths, in comparison to the planar structure. Oscillatory fringes in NW array spectra are due to complex interference in both vertical and horizontal directions. In reality, a NW array's sidewall roughness or random fluctuation in NW diameters and location can destroy the coherency of scattered light, leading to the absence of the oscillations in experimental spectra. This is one possible source for the discrepancy between theory and experiments, but it can be diminished by averaging out the simulated curves. In Fig. 31.8(a), the absorption values for a NW array consist of the absorption both in the NW arrays and in the substrate underneath. As expected, arrayed structures have substantially larger absorption due to a decrease of reflection caused by light scattering over patterned surfaces. However, when looking at the contribution of only the NW arrays ($1 - R - T_1$) in Fig. 31.8(b), the etched arrays do not absorb as much as do planar slabs with the same thickness. The discrepancy between the array and the slab decreases as the absorption length increases. This is, however, not contradictory to the general expectation stated at the beginning of the section. Considering that the NW arrays contain only ~20% of material volume compared to the planar slabs, absorption enhancement from light scattering indeed plays a large role. With longer NWs, scattered light inside the NW array has more chance to bounce back and forth between NWs and thus gets absorbed more than in shorter NWs. Therefore, it takes a smaller material volume in NW arrays to achieve the same amount of optical absorption in thin planar films. The advantage of a small material volume is the small number of thermally generated carriers, which, in turn reduces its component of dark current. For the same photocurrent generated from the same amount of light absorption, the decrease of dark current leads to an increase of open-circuit voltage in solar cells, as given by

$$V_{oc} = \frac{nkT}{q} \ln\left(\frac{I_{ph}}{I} + 1\right), \tag{31.12}$$

where

$$I = I_0 \left[\exp\left(\frac{qV}{nk_B T}\right) - 1\right]$$

is the bias-dependent dark current of a diffusion or generation–recombination-dominated photovoltaic device, n is the ideality factor, k_B is the Boltzmann constant, T is temperature, and I_0 is related to the number of minority carriers inside the devices, and this number is proportional to the material volume where the carriers are generated.

31.4.2 Effect of pitch size

The previous section emphasized the role of light scattering in the absorption of NW arrays. The question that follows is how one can strengthen the scattering process in order to obtain better absorption. As is well known in wave optics, scattering is more pronounced when the feature size approaches the light's wavelength. We thus may expect that it will be possible to enhance scattering by reducing the array's pitch size (distance between NWs). In order to evaluate the effect of scattering, we simulated NW arrays with pitch size p ranging from 1 to 5 μm. The NW length is kept the same at 3 μm, and the NW diameter is set at half of the pitch size so that the material filling ratio (NW cross-section area divided by unit cell area) is constant (~20%) in all cases.

As expected, the absorption spectra shown in Fig. 31.9(a) confirm stronger absorption for smaller pitch, where scattering is expected to be more pronounced. Enhancement at short wavelengths ($\lambda < 500$ nm) is more pronounced because at such wavelengths, the absorption coefficient is relatively high, the absorption occurs mostly at the surface, and the absorption magnitude is governed by the surface area at the silicon–air interfaces, rather than the material volume [Fig. 31.9(b)]. While, as we saw in Section 31.4.1, for large pitches, the absorption in the NW arrays is not as high as in a planar film of the same thickness; when the pitch is reduced to 1 μm, the scattering is so strong that the NW array absorption becomes larger than the reference thin film.

Figure 31.10 shows the absorption profile at $\lambda = 587$ nm in a 2D slice through the NW center in three different configurations ($p = 1$, 3, and 5 μm). The scale bars confirm once again that absorption occurs much more strongly

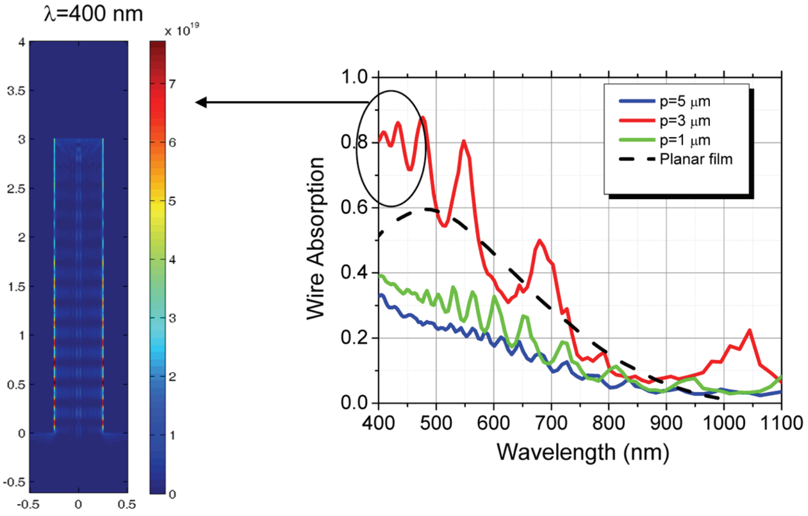

(a) (b)

Figure 31.9 (a) With an absorption profile at $\lambda = 400$ nm, the penetration depth is so small that the amount of absorption depends on the air–silicon surface area rather than on the volume of silicon. (b) Absorption spectra of silicon NW arrays with different pitches. (See color plate section.)

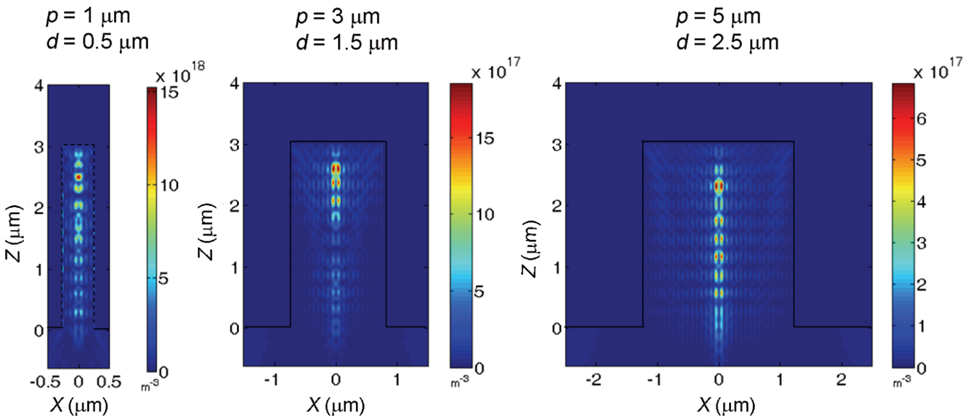

Figure 31.10 Spatial distribution of absorption in a cross-sectional slice through the NW center (note the increase of absorption magnitude in the scale bar for $p = 1$ μm). (See color plate section.)

in a smaller pitch than in a larger pitch. Another important remark drawn from Fig. 31.10 is that in all three cases the absorption occurs more strongly near the center of the NWs. This is as is expected because each individual NW acts as a waveguide for light propagation, making light intensity more concentrated in the center and, hence, resulting in a stronger absorption at the core.

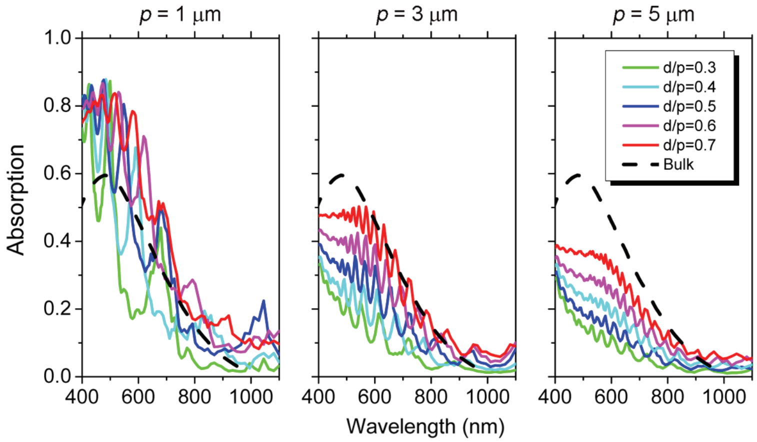

Figure 31.11 Absorption spectrum of NW arrays with different pitches and diameters. (See color plate section.)

Observations from Fig. 31.10 raise a question about the degree to which the outer part of the NW contributes to the total absorption. Figure 31.11 shows the absorption spectra of NW arrays with different diameter-to-pitch (d/p) ratios for the three pitches $p = 1$ μm, $p = 3$ μm, and $p = 5$ μm. For $p =$ 5 μm, the pitch is too large for the scattering effect to become dominant, the absorption is governed by the absorbing material volume; thus, the larger diameter has a higher absorption. With $p = 3$ μm, the effect of the material filling ratio is still dominant, resulting in the same trends as in $p = 5$ μm; however, the absorption is enhanced due to the presence of light scattering. For $p = 1$ μm, the scattering becomes so strong that the proportionality between absorption amplitude and material volume no longer holds. The scattered light deviates from normal incidence, bouncing back and forth between NWs and eventually becoming absorbed in the NWs rather than penetrating the substrate. Also, regardless of the NW diameter, the absorption is nearly the same.

The contribution of light scattering effects should be carefully considered while optimizing device performance. Ideally, a smaller pitch is desired to maximize enhanced absorption due to scattering. And at such a pitch, a small-diameter NW can still achieve high absorption while exhibiting low dark current due to smaller material volume. However, if technological limitation does not allow for small pitch and small diameter, and especially if the material is not of sufficient quality for the carrier diffusion lengths to be larger than the NW diameter, the design for *p–n* NWs will need to be carefully considered. For example, the core diameter should be small so that the junction is closer to the core where more carriers are generated from the absorption process. If permitted, the core material should be of *p* type, where the diffusion length of minority electrons is longer than that of holes in the *n*-type region; thus, generated electrons near the core have a higher chance of diffusing to the junction. In the absence of light scattering at a large pitch, larger NW diameters will result in stronger absorption at the expense of larger dark current. Compromises in terms of diameter and pitch will need to be taken into account for experimental optimizations.

In this work, arrays of cylindrical NWs are utilized for the simplicity and generality of the simulation; however, trends and interpretations can still be applied to other experimental configurations that slightly deviate from cylindrical form. In fact, advances in fabrication techniques can enable NW geometries that are more beneficial for the absorption process. Conical NWs[3] or dual-diameter structures[4] have been shown to enhance the absorbance to above 90%. The key in these works is the reduction of reflectance by minimizing the top flat areas that most strongly reflect the light. The growth conducted in this work has resulted in a different NW geometry that can lead to similar effects. During CVD shell deposition, crystalline spherical bulbs (so-called match heads) are built up at the top of the NWs due to faceted growth with different growth rates along different directions [Fig. 31.2(c)]. Not only is the reflection decreased due to literally no horizontal surface area, but the match heads also act as microlenses that converge incident light into the NW structure underneath, thus minimizing unabsorbed light penetrating into the substrate. Simulation shows that NW arrays with match heads have much higher absorption than similar arrays without match heads. Further details on

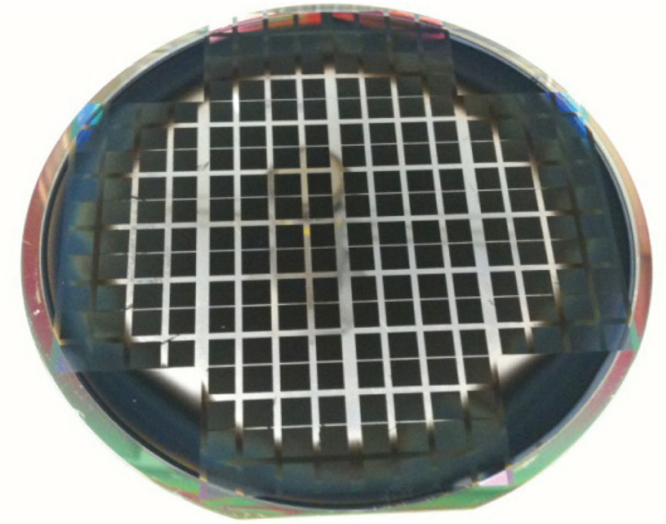

Figure 31.12 Optical photograph of a 6-in wafer with NW arrays fabricated using stepper photolithography and dry etching. ($L = 10$ μm, $d = 500$ nm, $p = 1.5$ μm.)

match head formation and their effects on optical absorption will be reported in a future publication.[16]

31.5 Conclusion and Outlook

Simulation results suggest that the optimal configuration for NW arrays is to minimize NW spacing (pitch) and diameter. Small NW spacing facilitates light scattering and thus enhances the absorption, even with short vertical absorption length. With small spacing, where light scattering is dominant, this approach does not need much material volume to totally absorb the incident light. However, in reality, it is still difficult to realize such a configuration with current technology. Small dimensions present extra challenges for both top-down core etching and CVD shell growth. One would have to compromise between the absorption efficiency dictated by array design and the electrical performance governed by the cleanness and dimensional limitations of the fabrication process. Using a nonoptimized design ($L = 7$ μm, $d = 1.65$ μm, and $p = 5$ μm), we have demonstrated a NW solar cell with 60% external quantum efficiency and 10% power conversion efficiency,[16] efficiencies that are comparable to the record values of efficiencies for NW solar cells at the time of this writeup.[12] It is expected that with further design optimization and further advances in fabrication to realize the theoretically optimized structure, the device efficiency should be considerably higher. An efficiency of 15% or above would have significant implications for the use of this NW approach for solar cells and would prove the approach to be a viable candidate in the market.

In addition to further pushing top-down etching to achieve small spacing and small diameters, the bottom-up approach to NW synthesis can be a viable alternative, considering the pros and cons of both methods for fabricating small NWs. VLS NWs can be grown with sub-100-nm diameters and do not suffer from small-spacing effects (on the order of few hundreds of nanometers), in contrast to those realized through top-down fabrication. Future improvements in NW verticality may become available with optimized growth conditions, and even in the nonoptimized case, slanted and touching NWs should not affect device performance because all NWs are electrically connected in parallel.

While research in NW solar cells is still at an early stage of demonstrating the capability of the system, the ultimate goal is to realize size-expandable, low-cost, high-performance cells. With the current fabrication scheme, the bottle neck for wafer scaling is the use of e-beam lithography for either mask formation in the top-down approach, or metal patterns in the bottom-up approach. However, such drawbacks can be easily overcome with alternative methods such as nanoimprint[19] or nanosphere photolithography,[20] or stepper photolithography. Thus, the present technology, once demonstrated, should be viable at large-scale production. For a proof of capability, the present authors have fabricated NW arrays over a 6-in wafer using stepper photolithography and dry etching (Fig. 31.12).

An effort to further reduce fabrication cost involves integrating NW solar cells onto low-cost alternative substrates. Compared to other solar cell technologies such as bulk silicon solar cells, NWs are more advantageous due to their arrayed structure where the gap between NWs makes the structure more flexible and can release stress arising from heterogeneous integration, especially for integration on flexible substrates. NW solar cells integrated on low-cost substrates have been shown by using direct CVD synthesis on an alternative substrate with a buffer layer,[6,21] and by embedding the NW array in a flexible polymer film for transferring to alternative substrates.[22,23] Although device performance of solar cells on foreign substrates is still limited, the large number of approaches to realize such devices and the rapid progress made in recent years suggest that NW solar cells may very well compete with existing planar technology.

Acknowledgments

This research was funded in part by the Laboratory Directed Research and Development program at Los Alamos National Laboratory and by the Department of Energy EERE (EB2102010). Work was performed in part at the Center for Integrated Nanotechnologies, a U.S. Department of Energy, Office of Basic Energy Sciences, user facility at Los Alamos National Laboratory (Contract DE-AC52-06NA25396).

References

1. B. M. Kayes, H. A. Atwater, and N. S. Lewis, “Comparison of the device physics principles of planar and radial *p–n* junction nanorod solar cells,” *J. Appl. Phys.* **97**(11), 114302–11 (2005).
2. L. Hu and G. Chen, “Analysis of optical absorption in silicon nanowire arrays for photovoltaic applications,” *Nano Lett.* **7**(11), 3249–3252 (2007).
3. J. Zhu, Z. Yu, G. F. Burkhard, C.-M. Hsu, S. T. Connor, Y. Xu, Q. Wang, M. McGehee, S. Fan, and Y. Cui, “Optical absorption enhancement in amorphous silicon nanowire and nanocone arrays,” *Nano Lett.* **9**(1), 279–282 (2008).
4. Z. Fan, R. Kapadia, P. W. Leu, X. Zhang, Y.-L. Chueh, K. Takei, K. Yu, A. Jamshidi, A. A. Rathore, D. J. Ruebusch, M. Wu, and A. Javey, “Ordered arrays of dual-diameter nanopillars for maximized optical absorption,” *Nano Lett.* **10**(10), 3823–3827 (2010).
5. E. Garnett and P. Yang, “Light trapping in silicon nanowire solar cells,” *Nano Lett.* **10**(3), 1082–1087 (2010).

6. L. Tsakalakos, J. Balch, J. Fronheiser, B. A. Korevaar, O. Sulima, and J. Rand, “Silicon nanowire solar cells,” *Appl. Phys. Lett.* **91**(23), 233117 (2007).
7. B. Tian, X. Zheng, T. J. Kempa, Y. Fang, N. Yu, G. Yu, J. Huang, and C. M. Lieber, “Coaxial silicon nanowires as solar cells and nanoelectronic power sources,” *Nature* **449**(7164), 885–889 (2007).
8. L. Yu, B. O’Donnell, P.-J. Alet, and P. Roca i Cabarrocas, “All-in-situ fabrication and characterization of silicon nanowires on TCO/glass substrates for photovoltaic application,” *Solar Energy Mater. Solar Cells* **94**(11), 1855–1859 (2010).
9. O. Gunawan and S. Guha, “Characteristics of vapor–liquid–solid grown silicon nanowire solar cells,” *Solar Energy Mater. Solar Cells* **93**(8), 1388–1393 (2009).
10. M. C. Putnam, S. W. Boettcher, M. D. Kelzenberg, D. B. Turner-Evans, J. M. Spurgeon, E. L. Warren, R. M. Briggs, N. S. Lewis, and H. A. Atwater, “Si microwire-array solar cells,” *Energy & Environ. Sci.* **3**(8), 1037–1041 (2010).
11. M. D. Kelzenberg, D. B. Turner-Evans, M. C. Putnam, S. W. Boettcher, R. M. Briggs, J. Y. Baek, N. S. Lewis, and H. A. Atwater, “High-performance Si microwire photovoltaics,” *Energy & Environ. Sci.* **4**(3), 866–871 (2011).
12. Y. Lu and A. Lal, “High-efficiency ordered silicon nano-conical-frustum array solar cells by self-powered parallel electron lithography,” *Nano Lett.* **10**(11), 4651–4656 (2010).
13. M. J. Naughton, K. Kempa, Z. F. Ren, Y. Gao, J. Rybczynski, N. Argenti, W. Gao, Y. Wang, Y. Peng, J. R. Naughton, G. McMahon, T. Paudel, Y. C. Lan, M. J. Burns, A. Shepard, M. Clary, C. Ballif, F. J. Haug, T. Söderström, O. Cubero, and C. Eminian, “Efficient nanocoax-based solar cells,” *physica status solidi–Rapid Res. Lett.* **4**(7), 181–183 (2010).
14. J.-Y. Jung, Z. Guo, S.-W. Jee, H.-D. Um, K.-T. Park, M. S. Hyun, J. M. Yang, and J.-H. Lee, “A waferscale Si wire solar cell using radial and bulk p–n junctions,” *Nanotechnol.* **21**(44), 445303 (2010).
15. S. T. Picraux, J. Yoo, I. H. Campbell, S. A. Dayeh, and D. E. Perea, “Semiconductor nanowires for solar cells,” in *Semiconductor Nanostructures for Optoelectronic Devices*, G.-C. Yi, Ed., Springer, Berlin-Heidelberg, pp. 297–328 (2012).
16. J. Yoo, S. A. Dayeh, W. Tang, and S. T. Picraux, “Epitaxial growth of radial Si p-i-n junctions for photovoltaic applications,” *Appl. Phys. Lett.* **102**(9), 093113–5 (2013).

17. Lumerical Solutions, Inc., FDTD Solutions, http://www.lumerical.com/.
18. E. D. Palik, *Handbook of Optical Constants of Solids*, Academic Press, San Diego (1998).
19. S. Y. Chou, P. R. Krauss, and P. J. Renstrom, "Imprint lithography with 25-nm resolution," *Science* **272**(5258), 85–87 (1996).
20. C. L. Haynes and R. P. Van Duyne, "Nanosphere lithography: A versatile nanofabrication tool for studies of size-dependent nanoparticle optics," *J. Phys. Chem. B* **105**(24), 5599–5611 (2001).
21. V. Sivakov, G. Andrä, A. Gawlik, A. Berger, J. Plentz, F. Falk, and S. H. Christiansen, "Silicon nanowire-based solar cells on glass: Synthesis, optical properties, and cell parameters," *Nano Lett.* **9**(4), 1549–1554 (2009).
22. K. E. Plass, M. A. Filler, J. M. Spurgeon, B. M. Kayes, S. Maldonado, B. S. Brunschwig, H. A. Atwater, and N. S. Lewis, "Flexible polymer-embedded Si wire arrays," *Adv. Mater.* **21**(3), 325–328 (2009).
23. L. V. Jayaraman, M. Ombaba, A. M. Katzenmeyer, and M. S. Islam, "Transfer of micro/nano-scale pillars and wires on conducting thermoplastic composite coated arbitrary substrates," *Proc. SPIE* **7683**, 768313 (2010) [doi: 10.1117/12.851762].

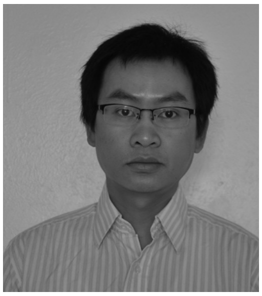

Binh-Minh Nguyen graduated from the Center for Quantum Devices, Northwestern University in 2010 and stayed as a Research Assistant Professor until he joined Los Alamos National Lab as a Director's Postdoctoral Fellow (2012). His research interests include band structure modeling, semiconductor device physics, epitaxial growth, nanofabrication, and materials and device characterizations. He currently focuses on exploring transport mechanisms in 1D Si/Ge nanowires, and developing novel electronic/optoelectronic devices. He has authored six book chapters and 59 papers with over 1000 citations. He serves as a frequent reviewer for many journals of IoP, AIP, OSA, and Elsevier. Nguyen was the recipient of SPIE scholarships in 2009 and 2010, an IEEE Photonics Society 2010 Fellowship, and the ECS's Edward Weston 2010 Summer Fellowship.

Shadi Dayeh received his Ph.D. degree in electrical engineering from the University of California San Diego in 2008. He joined Los Alamos National Laboratory as a Director Fellow in 2008 and was promoted to an Oppenheimer Fellow in 2010. In the Fall of 2012, he joined the faculty of Electrical and Computer Engineering at the University of California San Diego. His research work encompasses materials science and device physics for heterointegrated electronic and optoelectronic devices and systems and for bio-interface transducer devices.

S. Tom Picraux most recently served as Chief Scientist of the Center for Integrated Nanotechnologies (CINT) at Los Alamos National Laboratory, New Mexico, and currently is Lab Fellow Emeritus. Previously, he has served as a research scientist, manager, and center director at Sandia National Laboratories and as Executive Director for Materials Research and Professor at Arizona State University. Tom received his B.S. in electrical engineering from the University of Missouri-Columbia and his Ph.D. in engineering science & physics from the California Institute of Technology and studied physics at Cambridge University as a Fulbright Fellow. He is a past President of the Materials Research Society, past chair of the Division of Materials Physics of the American Physical Society, and past chair of the American Association for the Advancement of Science's Industrial Science and Technology Section. He is a Fellow of MRS, APS, AAAS, and Los Alamos National Laboratory, and received the U.S. Department of Education E.O. Lawrence Award for Materials Research. He has more than 325 publications, is the author of the book *Materials Analysis by Ion Channeling*, has edited 6 books, and has 16 book chapters with over 7000 citations. His research interests focus on ion-beam modification and analysis of materials, nanoscale electronic materials, and semiconducting nanowires.

Biographies for **Jinkyoung Yoo, Paul Schuele**, and **David Evans** are not available.